processes

MDPI

Article

Effect of Initial Salt Composition on Physicochemical and Structural Characteristics of Zero-Valent Iron Nanopowders Obtained by Borohydride Reduction

Denis Leybo *, Marat Tagirov *, Dmitry Arkhipov, Elizaveta Permyakova, Evgeny Kolesnikov and Denis Kuznetsov

National University of Science and Technology "MISiS", 119049 Moscow, Russia; arhipov.di@misis.ru (D.A.); permyakova.es@misis.ru (E.P.); kolesnikov.ea@misis.ru (E.K.); dk@misis.ru (D.K.)

* Correspondence: leybo.dv@misis.ru (D.L.); m1701562@edu.misis.ru (M.T.); Tel.: +7-499-237-2226 (D.L. & M.T.)

Received: 4 September 2019; Accepted: 18 October 2019; Published: 21 October 2019

Abstract: The effect of initial salt composition on characteristics of zero-valent iron nanopowders produced via borohydride reduction was studied. The samples were characterized by X-ray diffraction, scanning and transmission electron microscopy, and low-temperature nitrogen adsorption. The efficiency of Pb^{2+} ions removal from aqueous media was evaluated. The use of ferric salts led to enhanced reduction kinetics and, consequently, to a smaller size of iron particles in comparison with ferrous salts. A decrease in the ionic strength of the synthesis solutions resulted in a decrease in iron particles. The formation of small highly-reactive iron particles during synthesis led to their oxidation during washing and drying steps with the formation of a ferrihydrite phase. The lead ions removal efficiency was improved by simultaneous action of zero-valent iron and ferrihydrite phases of the sample produced from iron sulphate.

Keywords: nano zero-valent iron; borohydride reduction method; wastewater treatment; iron nanopowders; lead ions

1. Introduction

Wastewater is one of the main challenges of humanity in the 21st century. The fast growth of the population leads to the diminution of clean water reserves both because of increased global utilization and worsening of the ecological situation as a result of a constant increase in production. As mentioned in the United Nations (UN) World Water Development report [1], water demand is continuously increasing by 1% annually, and is expected to reach 6000 km^3 per year in 2050. About 80% of the water used by industry is released without any treatment [2], which puts the ecosystem and human health at risk.

Several chemical species have been identified as potentially harmful to human health. Among them are nitrates, fluorides, arsenic, and selenium, which constitute the main part of inorganic pollutants found in many locations around the world and are considered as the main priority chemicals for wastewater treatment technologies [3]. Other substances threatening human health include recalcitrant organic dyes [4], chlorinated organic compounds [5], phenolic compounds [6], and heavy metals (e.g., Cr, and Pb) [7–9]. Lead ions fall into wastewater mainly from the mining industry, smelters, hydroelectric power plants, among others [10]. The presence of lead in drinking water leads to irreversible health effects that can affect every organ of the human body [11]. The recommended limit concentration was set in the guidelines for drinking water as 0.01 mg/L for Pb(II) [12]; however, in industrial wastewaters, the lead-ion concentrations approach 200–500 mg/L [13]. Even though producers try to lower or exclude lead from manufacturing processes, lead is still used and exerts detrimental impact on the ecosystem [14].

So far different wastewater treatment technologies have been suggested, e.g., adsorption [15], biosorption [16,17], membrane technology [18,19], biodegradation [20,21], ion exchange [22,23], ionic liquid-based treatment [24]. Sorption methods have several advantages, such as high efficiency uptake for heavy metal ions at low concentrations, energy saving and easy sorbent synthesis [25]. Among these technologies are nano zero valent iron (nZVI)-based techniques that have gained much attention of some scientific groups [26]. nZVI particles showed superior efficiency in the removal of antibiotics [27], phenolic compounds [28], heavy metals [29,30], inorganic pollutants [31], and organic dyes [32,33]. Our previous studies showed that nZVI particles are very effective for the decomposition of azo dyes [34] and as a fenton-like zinc removal catalyst [35]. nZVI have a higher reaction rate because of their very high specific surface area and surface energy for the redox process [36]. The small particle size significantly increases the diffusion properties of the materials, reduces the required amount of sorbent [37], and reduces the required contact time between nZVI and water to prevent oxidation during the synthesis [38].

The primary method for the preparation of standalone and supported nZVI particles used by scientific groups is the borohydride reduction of iron ions [39]. Although this method has been used for several decades, it is still insufficiently studied in terms of different parameters that influence the properties of the final product. R. Eljamal et al. [40] reported the results of a comprehensive study of eight relevant experimental parameters, such as concentration, reaction temperature, pH, mixing speed, and reaction time on composition, particles' size and the surface area of the produced nZVI. Their findings resulted in some improvement of nitrate reduction efficiency by 27% and phosphorus adsorption by 9.5%. N. Goldstein et al. [41] studied the influence of the organophosphate stabilizers on nZVI particles' size and zeta potential. H. Woo et. al. [42] investigated the effect of a washing solution and drying condition on the reactivity of nanosized nZVI synthesized by borohydride reduction. However, up to date, there has been no information in the literature on the effect of initial salt composition on the properties of nZVI powders produced by the borohydride reduction method. Although the authors of [41] reported differences in the stabilization mechanisms using different organic additives for ferrous and ferric salts, it is still unclear how these salts affect the borohydride reduction of iron.

Another issue related to the method is the need to use a protective atmosphere to avoid oxidation of the as-prepared nZVI particles. This concern imposes restrictions on the widespread use of the method because of the increased complexity of the overall process. Thus, it is highly desirable to identify conditions that will allow producing nZVI in an ambient atmosphere.

Our research investigated the effect of ferric and ferrous salts choice on structural characteristics and the physicochemical properties of nZVI samples synthesized by borohydride reduction. The obtained samples were characterized by X-ray diffraction, scanning and transmission electron microscopy, and low-temperature nitrogen adsorption techniques. A tentative scheme of the initial salt effect was proposed based on the experimental results obtained in this work. The nZVI samples were evaluated in the process of Pb^{2+} ion removal from aqueous solution.

2. Materials and Methods

2.1. Materials

All the reagents ($FeSO_4 \cdot 7H_2O$, $Fe(NO_3)_3 \cdot 9H_2O$, $FeCl_2 \cdot 4H_2O$, $FeCl_3 \cdot 6H_2O$, sodium carboxymethylcellulose ($C_6H_7O_2(OH)_2CH_2COONa$), and $NaBH_4$) used in this work were of analytical grade and used without any additional purification. MilliQ water and absolute isopropanol were used for the synthesis and water purification experiments.

2.2. nZVI Synthesis

All the synthesis procedures were performed in an ambient atmosphere. The nZVI samples were obtained by the reduction of iron ions from different salts according to the following reactions [40,43]:

$$FeSO_4 + 2NaBH_4 + 6H_2O = Fe + Na_2SO_4 + 2B(OH)_3 + 7H_2 \quad (1)$$

$$Fe(NO_3)_3 + 3NaBH_4 + 9H_2O = Fe + 3NaNO_3 + 3B(OH)_3 + 10.5H_2 \quad (2)$$

$$FeCl_2 + 2NaBH_4 + 6H_2O = Fe + 2NaCl + 2B(OH)_3 + 7H_2 \quad (3)$$

$$FeCl_3 + 3NaBH_4 + 9H_2O = Fe + 3NaCl + 3B(OH)_3 + 10.5H_2 \quad (4)$$

In detail, 2.5 g of $FeSO_4 \cdot 7H_2O$/4 g of $Fe(NO_3)_3 \cdot 9H_2O$/2 g of $FeCl_2 \cdot 4H_2O$/2.7 g of $FeCl_3 \cdot 6H_2O$ were dissolved in 30 mL of deionized water. 30 mL of 10 wt. % $NaBH_4$ aqueous solution was added drop-by-drop for 10 min. Sodium borohydride was taken excessively to provide a complete reduction. The suspension was mixed during the next 30 min.

The precipitate was filtered through a 0.22 μm membrane filter; afterwards, it was washed from by-products with 250 mL of water and 250 mL of isopropanol, sequentially. The obtained sample was dried in a drying oven under vacuum at room temperature. For the sample obtained from iron nitrate, a possibility of passivating the nanoparticles' surface under the flow of 1% O_2/N_2 was also studied. For this experiment, the washing of the sample was performed in a Drexel flask with further drying under the flow of O_2/N_2 overnight. The washing of the sample, in this case, was done by decantation using a magnet to increase the sedimentation speed.

The reduction process was also performed in the presence of sodium carboxymethylcellulose (Na-CMC) [44] with Fe:Na-CMC molar ratio equal to 1:0.002, 1:0.0055, and 1:0.0108 to passivate the surface of iron nanoparticles obtained from $Fe(NO_3)_3 \cdot 9H_2O$ by the reaction (2). The precipitate was separated by vacuum filtration followed by washing with isopropanol (250 mL) and drying under vacuum at room temperature as in the previous experiments.

2.3. Characterization

The X-ray diffraction analysis (XRD) of the samples was done on Diffray 401 diffractometer (Scientific Instruments, Russia) operating with Cr-Kα radiation (λ = 2.2909 Å). The crystallites' size was estimated using the Scherrer equation, and the Si standard was used for instrumental broadening elimination. Scanning electron microscopy (SEM) and transmission electron microscopy (TEM) were used to study the morphology of the obtained particles. The SEM analysis was done on Tescan Vega 3 SB instrument, and the LEO 912 ab omega was used for the TEM analysis. The specific surface area analysis was performed using a low-temperature N_2 adsorption method with the Nova 1200e analyzer (Quantachrome, Boynton Beach, FL, USA) at 77 K. Before the analysis, the samples were degassed in vacuum at 120 °C for 3 h. The specific surface area was calculated using the Brunauer–Emmett–Teller (BET) equation.

The pH zero charge point (pH_{pzc}) was measured using the pH drift method [45,46]. Samples of 2.5 mg nZVI were introduced into a known volume (10 mL) of a solution of 0.1 M KNO_3. KNO_3 was selected as an inert electrolyte. The initial pH ($pH_{Initial}$) of the KNO_3 solutions was adjusted from 3 to 12 by adding 0.1 M HCl or NaOH solutions. Suspensions were left to balance for 24 h in closed vessels at room temperature. Then, the pH values (pH_{final}) were measured again. Based on the data obtained, we plotted the pH_{final} vs. $pH_{initial}$ dependence. pH_{pzc} was determined by the intersection with the $pH_{initial} = pH_{final}$ line.

2.4. Pb^{2+} Ions Removal

The water purification experiments were performed by measuring the concentration of Pb^{2+} ions in an aqueous solution in the presence of the nZVI samples reduced from different salts. In detail,

200 mL of 1.2 mM $Pb(NO_3)_2$ solution was mixed with 50 mg of nZVI. The suspension was processed in an ultrasonic bath for 10 min for homogenization. After the ultrasonic treatment, the suspension was left in a shaker for 230 min. The probes of the solutions were taken in 1-mL portions after 10 min of the ultrasonic treatment and after 10, 20, 50, 80, 110, 140, 170, 200, and 230 min of mechanical mixing for our further analysis of the Pb concentration. The concentration of Pb in the supernatant solutions was determined by inductively coupled plasma mass spectrometry on ICAP Q instrument (Thermoscientific) in triplicates.

The lead removal capacity q ($mg \cdot g^{-1}$) was calculated for the samples after treatment for 240 min by the following equation:

$$q = \frac{(C_0 - C_\tau) \cdot V}{m} \quad (5)$$

where C_0 is the initial concentration of Pb^{2+}, C_τ is the concentration of Pb^{2+} after 240 min of the experiment, V is the volume of the solution, and m is the mass of nZVI.

3. Results and Discussion

3.1. The Effects of Initial Salt on the Phase Composition of the nZVI Samples

The X-ray diffraction patterns of the powders obtained after the reduction of iron with sodium borohydride from $FeSO_4$, $FeCl_2$, and $FeCl_3$ had characteristic peaks at 2θ angles equal to 68.6° and 106.0°, corresponding to metallic iron (Figure 1, PDF card no. 06-0696). The data confirmed that iron precipitated in a zero valence state. The sample obtained from $FeSO_4$ also contained the 2-line ferrihydrite (Fh) phase, $Fe_{10}O_{14}(OH)_2$ [47], which was confirmed by the presence of the broad peaks at 2θ angles equal to 52.6° and 99.5° [48]. nZVI could not be obtained by reducing Fe^{3+} ions from $Fe(NO_3)_3$ with $NaBH_4$. This sample consisted of only the Fh phase. The XRD patterns show that the iron particles reduced from $FeCl_2$ had the highest crystallinity (Figure 1), which was confirmed by the lowest full width at half maximum (FWHM) value.

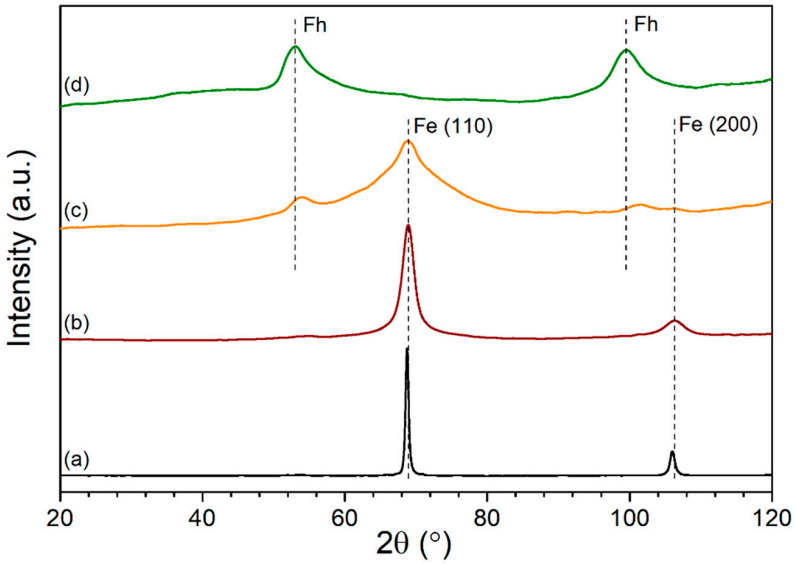

Figure 1. The X-ray diffraction analysis (XRD) patterns of powders obtained by reduction from $FeCl_2$ (**a**); $FeCl_3$ (**b**); $FeSO_4$ (**c**); $Fe(NO_3)_3$ (**d**).

The XRD pattern in Figure 1 shows that the best results were obtained by reducing iron from its chlorides. The content of the oxidized products in the final samples obtained from different salts decreased in the series $Fe(NO_3)_3 > FeSO_4 > FeCl_3 \approx FeCl_2$.

The ferrihydrite phase is usually synthetically produced by hydrolyzing ferric or ferrous salts [48]. Our observations on suspension's color change during the reduction of the iron nitrate salt suggested

that the formation of the Fh phase occurred after the end of the reduction process, which means that this was a secondary product of the iron particles oxidation. H. Pullin et al. [49] observed the formation of the Fh phase as a corrosion product of the nZVI particles in aqueous media. The authors stated that the formation of 2-line ferrihydrite, being intermediate to more stable iron oxide and oxohydroxide phases, was detectable during the entire experiment lasting for more than four weeks. Similar results were obtained by A. Liu et al. [50] during their study of the nZVI composition evolution in static water after ten days of the experiment.

The corrosion rate of nZVI is inversely proportional to the size of the particles comprising the powder. The results obtained in our work indicate the dependence of the final product composition on the initial salt used for the production of nZVI, which could be attributed to the different sizes of the particles formed during the synthesis. Thus, the use of iron nitrate led to the formation of extremely reactive small iron particles stable only under reductive conditions. The iron sulphate-derived sample only partially consisted of the Fh phase, which suggested the formation of more stable and larger particles during the borohydride reduction; whereas the use of iron chlorides allowed producing the pure iron phase.

During the reduction of the iron ions from the nitrate salt, the color change of the suspension from black to rusty was observed during the drying step. Thus, an additional experiment on the passivation of the surface of the iron particles reduced from nitrate during drying using an O_2/N_2 mixture was conducted to protect against oxidation. The XRD pattern of this sample is shown in Figure 2a. It can be seen from the results that the only crystalline phase present in the sample was sodium borate. Sodium borate forms as a by-product of the sodium borohydride hydrolysis reaction [51] and are usually removed during the washing procedure. The decantation is less efficient for the sample purification. The rusty color of the sample suggested that it should contain iron-based compounds, probably, in a low crystallinity form. To confirm this, the energy dispersive X-ray (EDX) analysis of the sample was done. The results (Figure 2b) show that the sample contained iron, most probably, in the form of the amorphous Fh phase. Therefore, this route is inappropriate for the production of nZVI.

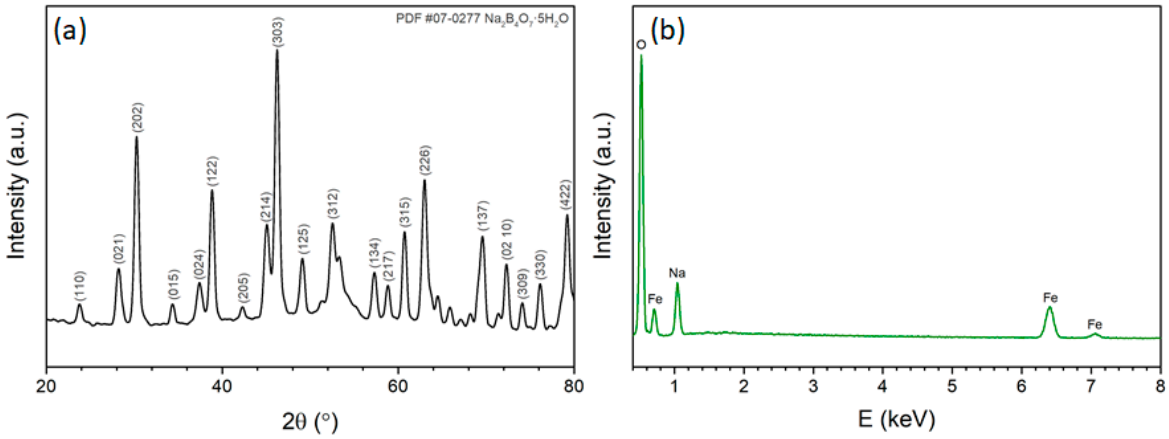

Figure 2. The XRD pattern (**a**) and the energy dispersive X-ray (EDX) analysis (**b**) of the powder obtained by reduction from $Fe(NO_3)_3$ with passivation in a current of 1% O_2/N_2 in a Drexel bottle.

The second route for stabilizing the surface of the iron particles reduced from the nitrate salt in this work was the usage of Na-CMC as an additive. Sodium CMC is known to be soluble in water and poorly soluble in alcohols. Thus, changing the solvent during the washing procedure could result in the formation of the Na-CMC protective coating on the surface of the iron particles. The XRD pattern in Figure 3 shows that all the samples obtained using the sodium CMC as a passivating agent consisted of ferrihydrite phase. The results obtained in this work show that it is impossible to produce nZVI with a sodium borohydride reduction of the nitrate salt using the abovementioned techniques.

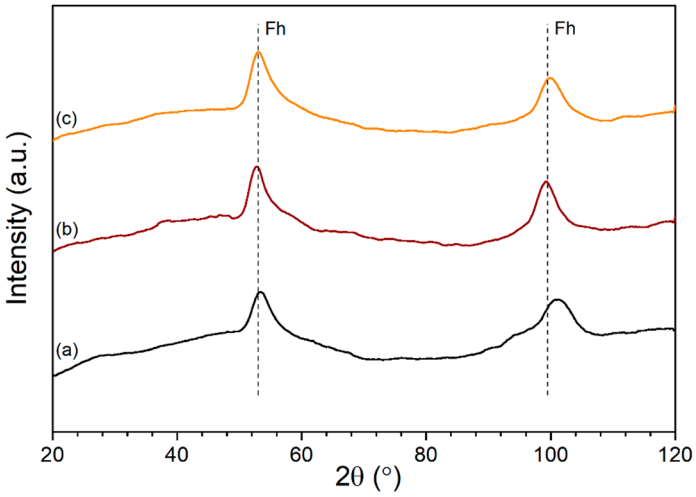

Figure 3. The XRD patterns of the powders obtained by reduction from $Fe(NO_3)_3$ with a concentration of CMC 1:0.002 (**a**), 1:0.0055 (**b**), and 1:0.0108 (**c**).

3.2. The Effects of Initial Salt on Structural Characteristics of Iron-Based Samples

3.2.1. SEM Results

The SEM images of nanoparticles are shown in Figure 4. The nZVI particles reduced from $FeSO_4$ formed aggregates of complex shapes (Figure 4a). The SEM images of the powder reduced from $Fe(NO_3)_3$ showed aggregates of the particles with an extended surface (Figure 4b). The image revealed that these aggregates consist of flake-shaped particles. The particles of the iron sample produced from $FeCl_2$ and $FeCl_3$ were arranged in chains (Figure 4c,d). The particle size of the sample produced from $FeSO_4$ was approximately 50–60 nm, the cross-section particle size of the sample produced from $FeCl_2$ was approximately 70–90 nm and of $FeCl_3$ 30–45 nm. The aggregates of the particles obtained from $Fe(NO_3)_3$ had sizes in a range from 500 nm to 1 µm.

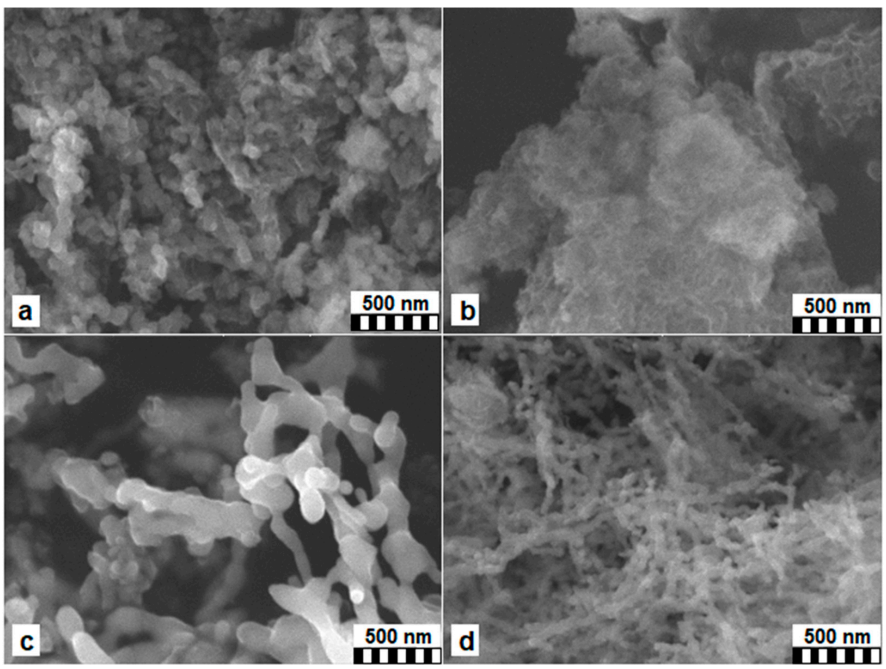

Figure 4. The scanning electron microscopy (SEM) images of nZVI produced from $FeSO_4$ (**a**), $Fe(NO_3)_3$ (**b**), $FeCl_2$ (**c**), $FeCl_3$ (**d**).

3.2.2. TEM Results

The TEM images of the nanoparticles are shown in Figure 5. The aggregates of the nZVI particles obtained from $FeSO_4$ had a developed morphology (Figure 5a). The sample consisted of flake-like particles as well as particles of an irregular form with a size of around 20 nm. The TEM images of the powder produced from $Fe(NO_3)_3$ showed that two-dimensional structures with a thickness of about 2 nm were obtained (Figure 5b). The nZVI particles obtained from $FeCl_2$ and $FeCl_3$ were arranged in chains and had a core-shell structure with a shell thickness of about 3–6 nm (Figure 5c,d). The particles' size of the iron samples reduced from $FeCl_2$ was approximately 100 nm, and from $FeCl_3$ was 20–30 nm.

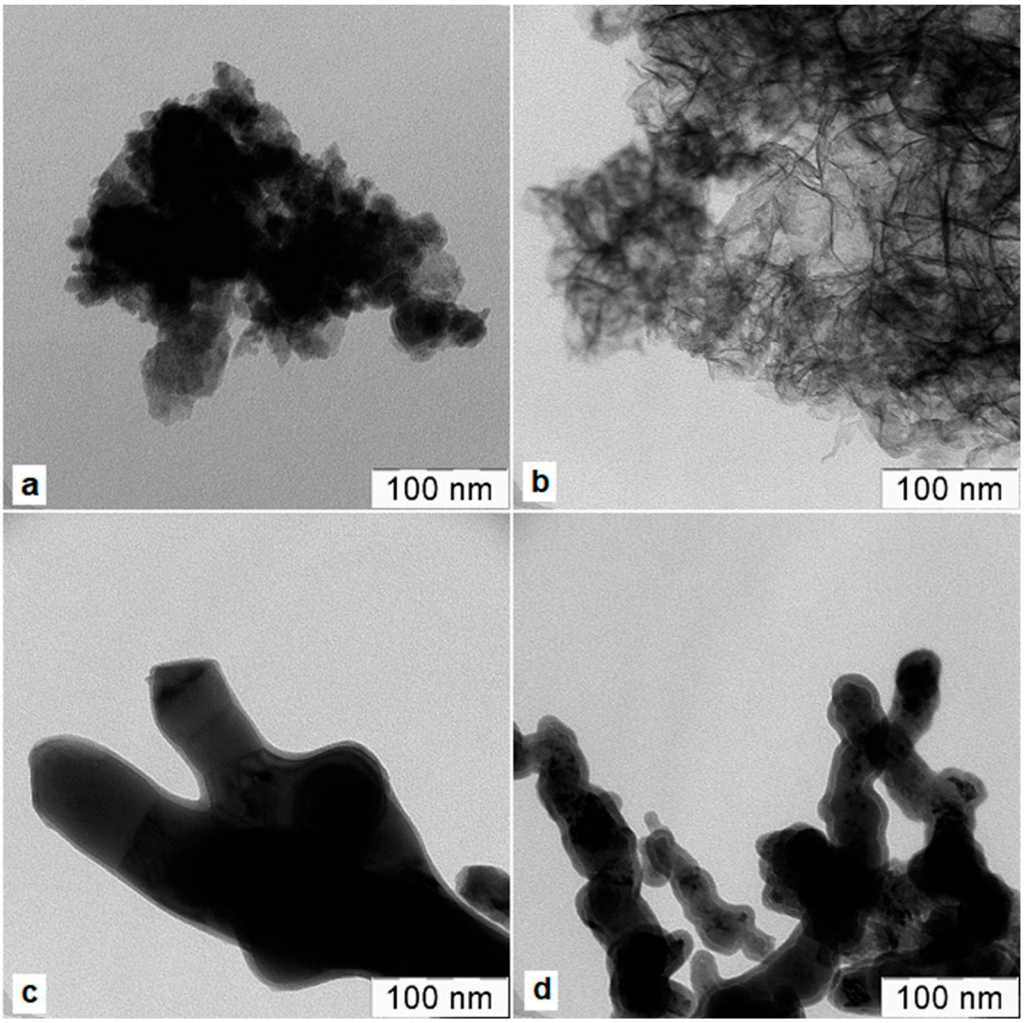

Figure 5. The transmission electron microscopy (TEM) images of nZVI produced from $FeSO_4$ (**a**), $Fe(NO_3)_3$ (**b**), $FeCl_2$ (**c**), $FeCl_3$ (**d**).

The results of the morphology study of the nZVI samples obtained in this work are well correlated with their composition and the results obtained by other authors. The 2D structures produced using the iron nitrate salt are characteristic of ferrihydrite being a poorly crystalline iron compound with the crystallites' size of 2–6 nm [52–54]. The structures similar to the obtained ones via the reduction of iron sulphate in this work were also observed by different researchers [55,56]. Mainly, these structures were assigned to the presence of iron oxides [57] on the surface of the Fe^0 particles. Our results showed that these structures correspond to the formation of ferrihydrite via oxidation of small reactive iron particles. The core-shell structured chains of the nZVI aggregates are the most commonly encountered morphology of iron produced by a borohydride reduction process [30,58,59]. The shell composition

according to the XPS analysis was shown to be Fe_2O_3 [59], the most stable iron oxide, comprising the passivation coating preventing their fast oxidation upon exposure to air/water environment.

3.2.3. Specific Surface Area and Crystallites' Size

The specific surface area and the crystallites' sizes of the iron samples reduced from various salts are presented in Table 1.

Table 1. The characteristics of the recovered powders.

Initial Salt	Phase Composition	S_{sp}, m^2/g	Crystallites' Size, nm
$FeSO_4$	Fe, Fh	73.0	5.6
$Fe(NO_3)_3$	Fh	277.3	-
$FeCl_2$	Fe	6.2	108.1
$FeCl_3$	Fe	46.3	11.7

The powder produced from iron nitrate had the largest surface area among the samples. The smallest specific surface area was identified for iron particles reduced from $FeCl_2$. The obtained results are in good agreement with the particles' size and the morphology observations visible on the SEM and TEM images. Thus, the 2D morphology of the particles produced from $Fe(NO_3)_3$ salt resulted in the highest surface area. The presence of such two-dimensional structures in the sample produced from sulphate was also responsible for the high surface area of this sample. Because both samples containing 2D structures consisted of Fh, we could conclude that the particles of such morphology corresponded to the Fh phase. In the case of the iron chloride salts, the largest specific surface area was obtained for the powder produced from $FeCl_3$, which is well correlated to the smaller size of the particles produced from this salt.

The crystallites' size for the iron particles reduced from $FeSO_4$ had the smallest value among the samples although it could be underestimated because of the presence of the amorphous phase in the sample. The powders obtained from $FeCl_2$ had the largest crystallites' size, almost ten times larger than those reduced from the $FeCl_3$ salt. The comparison of these values with a transverse size of the particles measured from the SEM and TEM images led us to the conclusion that the chain aggregates produced from the iron chloride salts consisted of single-crystal domains of iron.

3.3. The Scheme of Initial Salt Composition Effect on Reduction of Fe Ions

The sodium borohydride reduction of iron was performed using Fe^{3+} and Fe^{2+} containing salts in present work according to the reactions [55,58]:

$$Fe^{2+} + 2BH_4^- + 6H_2O = Fe^0 + 2B(OH)_3 + 7H_2 \quad (6)$$

$$Fe^{3+} + 3BH_4^- + 9H_2O = Fe^0 + 3B(OH)_3 + 10.5H_2 \quad (7)$$

The standard reduction potentials of these ions are different, with Fe^{2+} having a more negative value of −0.447 V in comparison with −0.037 V for Fe^{3+} ion. Consequently, it is easier to reduce ferric ion [60] from the solution. Since we can expect that iron ions form identical transition complexes [43], the rate constant of the reaction (6) is higher, which leads to the formation of smaller particles using ferric ion as the source of iron.

Among the salts containing identical iron ions the difference in the properties of the produced iron powders originates from the corresponding anions. Although the anions do not participate in the reactions (5) and (6) directly, they do form the ionic atmosphere that influences the reaction rate. According to the Brönsted–Bjerrum equation [61], an increase in the ionic strength of the solution results in a decrease of the reaction rate constant when the reacting ions have different signs. Thus, the formation of smaller iron particles is more favorable in the solutions of lower ionic strength.

Taking into account the abovementioned qualitative relationships, a tentative scheme of the initial salt composition effect on the reduction of Fe ions is proposed in this work (Figure 6). According to the scheme, the use of ferric ion-containing $FeCl_3$ and $Fe(NO_3)_3$ salts leads to the formation of smaller particles during the reduction process as compared to the $FeCl_2$ and $FeSO_4$. The ionic strength of the solutions used in this work was calculated to be equal (in mol/L) to 1.8, 2.0, 2.4, and 2.6 for $FeSO_4$, $FeCl_2$, $Fe(NO_3)_3$, and $FeCl_3$ initial salts, respectively. The iron particle formation rate is higher for the $FeSO_4$ and $Fe(NO_3)_3$ initial salts due to their lower ionic strengths. After the formation of nZVI during the washing and drying steps, small highly reactive particles are oxidized by water and dissolved oxygen with the formation of the Fh phase in the case of $Fe(NO_3)_3$ and, partially, $FeSO_4$ salts. Larger nZVI particles produced from the chlorides agglomerate in the chain structures with the formation of a passivation oxide layer on their surface.

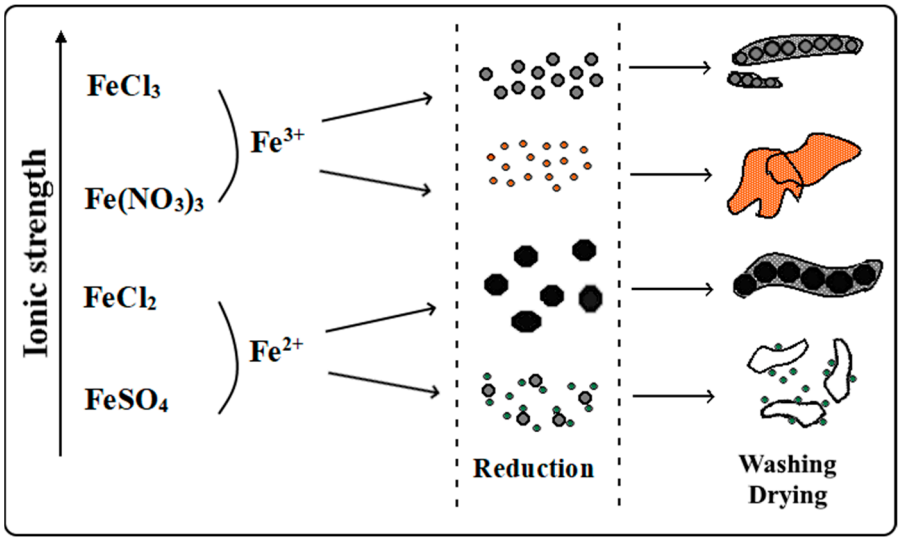

Figure 6. The scheme of the nZVI production via a borohydride reduction of different salts.

3.4. The Effects of Initial Salt Composition to Pb^{2+} Ions Removal Efficiency

The results of the removal of Pb^{2+} ions removal are illustrated in Figure 7. The horizontal axis shows the total processing time as the sum of the ultrasonic and mechanical treatment. The concentration of the Pb^{2+} ions rapidly decreased after the ultrasonic treatment for the nZVI samples obtained from all the salts. Then there was a gradual decrease in the concentration of all the samples within the next 120 min. There was a relatively slight fluctuation after 120 min of the experiment. The lead removal capacity q was equal to 744, 646, 462, and 650 $mg \cdot g^{-1}$ for the nZVI samples obtained from $FeSO_4$, $Fe(NO_3)_3$, $FeCl_2$, and $FeCl_3$, respectively, after the treatment for 240 min. Interestingly, the nZVI sample obtained from $FeSO_4$ showed maximum efficiency in the removal of the Pb^{2+} ions as compared to other nZVI samples.

Table 2 shows the comparison of the lead removal capacity results obtained in the present study and by other authors. Zhang Dongsheng et al. [30] gave q calculations for the removal of lead from the obtained nZVI and nZVI powders after freeze-drying. Chuang Yu et al. [62] reported the results of the adsorption of lead ions by GO-B-nZVI composite. Humera Jabeen et al. [63] in their work compared the adsorption capacity q for the synthesized powders of nZVI and composites based on graphene and nZVI (G-nZVI).

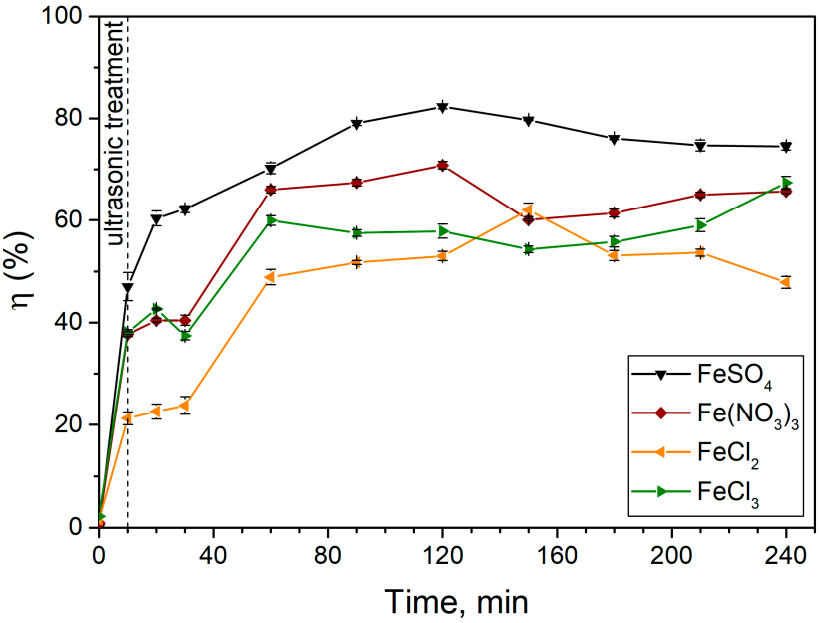

Figure 7. Pb^{2+} ions removal efficiency by the nZVI samples produced from different salts.

Table 2. Comparison of the lead removal capacity results.

Material	q, mg*g^{-1}	Reference
nZVI	855	[30]
nZVI-drying	758	[30]
GO-B-nZVI	199	[62]
nZVI	133	[63]
G-nZVI	181	[63]
nZVI from $FeSO_4$	744	this work
nZVI from $Fe(NO_3)_3$	646	this work
nZVI from $FeCl_2$	463	this work
nZVI from $FeCl_3$	650	this work

The comparison of the results with the characteristics of the samples obtained in this work reveals that there was a synergy between Fh and zero-valent iron, which led to the increased efficiency of the lead removal. Thus, the removal of the lead ions by the iron chloride originated samples was lower, which can be attributed to lower suspension stability of the nZVI particles in the solution as well as the lower specific surface area of these samples. These samples consisted of iron in a metallic form. The sample obtained from the iron nitrate had moderate efficiency. Although this sample did not contain zero-valent iron, its high specific surface area resulted in high adsorption capacity. The composition of the nZVI sample produced from sulphate ensured its high efficiency as a result of both positive actions of zero-valent iron capable of reducing lead ions [30] and ferrihydrite phase providing high surface area and the suspension stability of this sample.

Three mechanisms leading to the removal of lead ions from an aqueous solution are considered to be the main ones: sorption, reduction, and coprecipitation. During Pb^{2+} ions removal experiments, the initial pH was 4.53 for all samples. The final pH also did not differ significantly and varied in the series 5.54, 5.52, 5.51, 5.48 for $FeSO_4$, $Fe(NO_3)_3$, $FeCl_2$, and $FeCl_3$, respectively. An increase in pH is associated with the oxidation of nZVI in an acid solution. A relatively small change in pH during the

removal of lead ions indicates a slight contribution of the coprecipitation mechanism on the overall Pb ions removal.

An important characteristic of nZVI is the point of zero charge (pH_{pzc}). pH_{pzc} is the pH at which the number of positively and negatively charged centers on the surface of the powder is the same. If $pH < pH_{pzc}$, part of the protons from the solution is adsorbed on the surface with the formation of a positive charge, part of the counterions (OH^-) in the surface layer of the solution will be released and the pH of the contacting solution will increase, approaching pH_{pzc}; otherwise, some OH^- groups will sorb, and the surface will acquire a negative charge.

The results of determining pH_{pzc} for nZVI samples are presented in Figure 8. The dashed line shows the position where $pH_{initial} = pH_{final}$. pH_{pzc} was determined by the intersection of the graphs with a dashed line. pHpzc were 7.9, 6.6, 9.1, and 8.8 for the nZVI samples obtained from $FeSO_4$, $Fe(NO_3)_3$, $FeCl_2$, and $FeCl_3$, respectively. The pH_{pzc} of the obtained nZVI samples are not favorable for the electrostatic adsorption of Pb^{2+} cations. Therefore, adsorption also does not make a priority contribution to the removal of the lead ions.

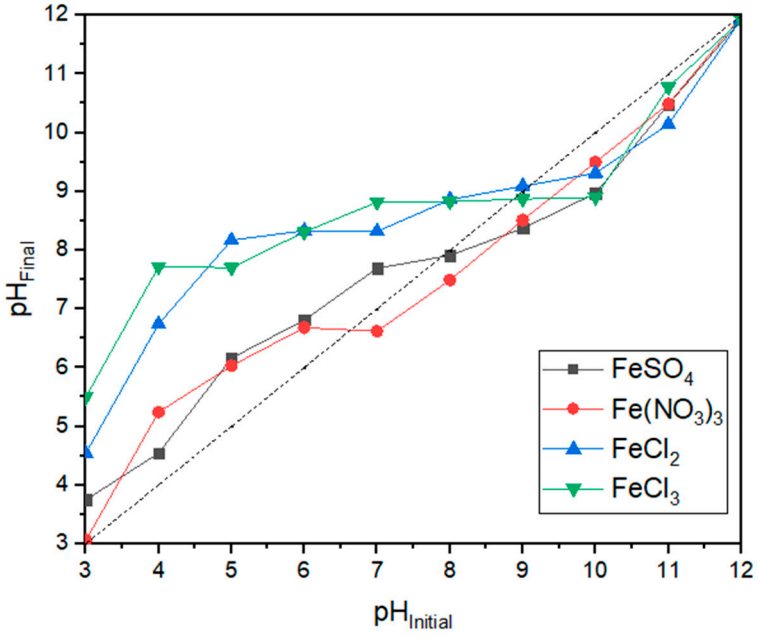

Figure 8. pH_{final} versus $pH_{initial}$ during equilibration of nZVI powders in 0.1 M KNO_3 solution.

The obtained results of measuring the pH of the solution and pH_{pzc} of nZVI samples show that the processes of coprecipitation and electrostatic adsorption were not the main ones during the removal of Pb^{2+} ions from the aqueous environment. Apparently, the reduction of Pb^{2+} ions by nZVI made a predominant contribution to the process of water purification from lead ions.

4. Conclusions

Iron-based samples with different phase compositions, particles' size, and morphology can be obtained by a borohydride reduction of various ferric and ferrous iron salts. The use of ferric salts leads to the formation of smaller iron particles during the synthesis because of a higher value of the reduction potential and the enhanced reaction kinetics. The formation of such highly reactive particles results in their further oxidation by water and dissolved oxygen with the formation of 2D ferrihydrite. The oxidation cannot be avoided by O_2/N_2 passivation and Na-CMC assisted synthesis. Among the salts containing iron ions with the same oxidation state the difference in the corresponding nZVI samples' characteristics originated from different solution's ionic strength, which influences the reduction rate.

The synergistic action of zero-valent iron and ferrihydrite leads to superior Pb^{2+} ion removal from water. This effect is easily achieved by the borohydride reduction of iron from sulphate salt.

Pure ferrihydrite shows moderate lead ion removal efficiency despite the highest specific surface area among the samples since the adsorption is the only action mechanism. The phase pure zero-valent iron samples have the lowest Pb^{2+} ions removal efficiency because of the lowest suspension stability and the adsorption capacity.

Author Contributions: Conceptualization, D.K.; formal analysis, D.L.; funding acquisition, D.A.; investigation, D.L. and M.T.; methodology, D.L., M.T., E.P., and E.K.; project administration, D.A.; supervision, D.K.; visualization, M.T.; writing–original draft, D.L. and M.T.; writing–review and editing, D.L., M.T., and D.K.

Funding: RFBR funded the reported study according to the research project No. 18-29-25051.

Conflicts of Interest: The authors declare no conflict of interest.

References

1. UN. *The United Nations World Water Development Report 2018: Nature-Based Solutions for Water*; UN: Paris, France, 2018.
2. UN. *The United Nations World Water Development Report 2017. Wastewater: The Untapped Resource*; UN: Paris, France, 2017.
3. Thompson, T.; Fawell, J.; Kunikane, S.; Jackson, D.; Appleyard, S.; Callan, P.; Bartram, J.; Kingston, P. *Chemical Safety of Drinking Water: Assessing Priorities for Risk Management*; WHO: Geneva, Switzerland, 2007.
4. Rovira, J.; Domingo, J.L. Human health risks due to exposure to inorganic and organic chemicals from textiles: A review. *Environ. Res.* **2019**, *168*, 62–69. [CrossRef]
5. Huang, B.; Lei, C.; Wei, C.; Zeng, G. Chlorinated volatile organic compounds (Cl-VOCs) in environment—Sources, potential human health impacts, and current remediation technologies. *Environ. Int.* **2014**, *71*, 118–138. [CrossRef] [PubMed]
6. Raza, W.; Lee, J.; Raza, N.; Luo, Y.; Kim, K.H.; Yang, J. Removal of phenolic compounds from industrial waste water based on membrane-based technologies. *J. Ind. Eng. Chem.* **2019**, *71*, 1–18. [CrossRef]
7. Sharma, S.; Nagpal, A.K.; Kaur, I. Appraisal of heavy metal contents in groundwater and associated health hazards posed to human population of Ropar wetland, Punjab, India and its environs. *Chemosphere* **2019**, *227*, 179–190. [CrossRef] [PubMed]
8. Mao, C.; Song, Y.; Chen, L.; Ji, J.; Li, J.; Yuan, X.; Yang, Z.; Ayoko, G.A.; Frost, R.L.; Theiss, F. Human health risks of heavy metals in paddy rice based on transfer characteristics of heavy metals from soil to rice. *Catena* **2019**, *175*, 339–348. [CrossRef]
9. Rai, P.K.; Lee, S.S.; Zhang, M.; Tsang, Y.F.; Kim, K.H. Heavy metals in food crops: Health risks, fate, mechanisms, and management. *Environ. Int.* **2019**, *125*, 365–385. [CrossRef]
10. Gorchev, H.G.; Ozolins, G. *Guidelines for Drinking-Water Quality*; WHO: Geneva, Switzerland, 2011; Volume 1, p. 564.
11. Ahamed, M.; Akhtar, M.J.; Alhadlaq, H.A. Preventive effect of TiO2 nanoparticles on heavy metal Pb-induced toxicity in human lung epithelial (A549) cells. *Toxicol. Vitr.* **2019**, *57*, 18–27. [CrossRef]
12. Pandey, R.; Dwivedi, M.K.; Singh, P.K.; Patel, B.; Pandey, S.; Patel, B.; Patel, A.; Singh, B. Effluences of Heavy Metals, Way of Exposure and Bio-toxic Impacts: An Update. *J. Chem. Chem. Sci.* **2016**, *66*, 2319–7625.
13. Arbabi, M.; Hemati, S.; Amiri, M. Removal of lead ions from industrial wastewater: A review of Removal methods. *Int. J. Epidemiol. Res.* **2015**, *2*, 105–109.
14. Wani, A.L.; Ara, A.; Usmani, J.A. Lead toxicity: A review. *Interdiscip. Toxicol* **2015**, *8*, 55–64. [CrossRef]
15. Sharma, A.; Syed, Z.; Brighu, U.; Gupta, A.B.; Ram, C. Adsorption of textile wastewater on alkali-activated sand. *J. Clean. Prod.* **2019**, *220*, 23–32. [CrossRef]
16. Lapo, B.; Demey, H.; Zapata, J.; Romero, C.; Sastre, A. Sorption of Hg (II) and Pb (II) ions on chitosan-iron (III) from aqueous solutions: Single and binary systems. *Polymers* **2018**, *10*, 367. [CrossRef] [PubMed]
17. Demey, H.; Melkior, T.; Chatroux, A.; Attar, K.; Thiery, S.; Miller, H.; Marchand, M. Evaluation of torrefied poplar-biomass as a low-cost sorbent for lead and terbium removal from aqueous solutions and energy co-generation. *Chem. Eng. J.* **2019**, *361*, 839–852. [CrossRef]
18. Abdel-Fatah, M.A. Nanofiltration systems and applications in wastewater treatment: Review article. *Ain Shams Eng. J.* **2018**, *9*, 3077–3092. [CrossRef]

19. Sunil, K.; Karunakaran, G.; Yadav, S.; Padaki, M.; Zadorozhnyy, V.; Pai, R.K. Al-Ti_2O_6 a mixed metal oxide based composite membrane: A unique membrane for removal of heavy metals. *Chem. Eng. J.* **2018**, *348*, 678–684. [CrossRef]
20. Yang, L.; Sheng, M.; Zhao, H.; Qian, M.; Chen, X.; Zhuo, Y.; Cao, G. Treatment of triethyl phosphate wastewater by Fenton oxidation and aerobic biodegradation. *Sci. Total Environ.* **2019**, *678*, 821–829. [CrossRef]
21. Goswami, L.; Kumar, R.V.; Pakshirajan, K.; Pugazhenthi, G.A. A novel integrated biodegradation—Microfiltration system for sustainable wastewater treatment and energy recovery. *J. Hazard. Mater.* **2019**, *365*, 707–715. [CrossRef]
22. Mohammadtabar, F.; Pillai, R.G.; Khorshidi, B.; Hayatbakhsh, A.; Sadrzadeh, M. Efficient treatment of oil sands produced water: Process integration using ion exchange regeneration wastewater as a chemical coagulant. *Sep. Purif. Technol.* **2019**, *221*, 166–174. [CrossRef]
23. Muhammad, A.; Soares, A.; Jefferson, B. The impact of background wastewater constituents on the selectivity and capacity of a hybrid ion exchange resin for phosphorus removal from wastewater. *Chemosphere* **2019**, *224*, 494–501. [CrossRef]
24. Isosaari, P.; Srivastava, V.; Sillanpää, M. Ionic liquid-based water treatment technologies for organic pollutants: Current status and future prospects of ionic liquid mediated technologies. *Sci. Total Environ.* **2019**, *690*, 604–619. [CrossRef]
25. Attar, K.; Demey, H.; Bouazza, D.; Sastre, A.M. Sorption and desorption studies of Pb (II) and Ni (II) from aqueous solutions by a new composite based on alginate and magadiite materials. *Polymers* **2019**, *11*, 340. [CrossRef] [PubMed]
26. Crane, R.A.; Scott, T.B. Nanoscale zero-valent iron: Future prospects for an emerging water treatment technology. *J. Hazard. Mater.* **2012**, *211*, 112–125. [CrossRef] [PubMed]
27. Pirsaheb, M.; Moradi, S.; Shahlaei, M.; Wang, X.; Farhadian, N. A new composite of nano zero-valent iron encapsulated in carbon dots for oxidative removal of bio-refractory antibiotics from water. *J. Clean. Prod.* **2019**, *209*, 1523–1532. [CrossRef]
28. Bavandi, R.; Emtyazjoo, M.; Saravi, H.N.; Yazdian, F.; Sheikhpour, M. Study of capability of nanostructured zero-valent iron and graphene oxide for bioremoval of trinitrophenol from wastewater in a bubble column bioreactor. *Electron. J. Biotechnol.* **2019**, *39*, 8–14. [CrossRef]
29. Zhang, W.; Oswal, H.; Renew, J.; Ellison, K.; Huang, C.H. Removal of heavy metals by aged zero-valent iron from flue-gas-desulfurization brine under high salt and temperature conditions. *J. Hazard. Mater.* **2019**, *373*, 572–579. [CrossRef] [PubMed]
30. Zhang, D.; Gao, W.; Chang, G.; Luo, S.; Jiao, W.; Liu, Y. Removal of heavy metal lead (II) using nanoscale zero-valent iron with different preservation methods. *Adv. Powder Technol.* **2019**, *30*, 581–589. [CrossRef]
31. Yan, W.; Herzing, A.A.; Kiely, C.J.; Zhang, W.X. Nanoscale zero-valent iron (nZVI): Aspects of the core-shell structure and reactions with inorganic species in water. *J. Contam. Hydrol.* **2010**, *118*, 96–104. [CrossRef]
32. Xu, J.; Wang, X.; Pan, F.; Qin, Y.; Xia, J.; Li, J.; Wu, F. Synthesis of the mesoporous carbon-nano-zero-valent iron composite and activation of sulfite for removal of organic pollutants. *Chem. Eng. J.* **2018**, *353*, 542–549. [CrossRef]
33. Zhang, M.H.; Dong, H.; Zhao, L.; Wang, D.X.; Meng, D. A review on Fenton process for organic wastewater treatment based on optimization perspective. *Sci. Total Environ.* **2019**, *670*, 110–121. [CrossRef]
34. Mikhailov, I.; Levina, V.; Leybo, D.; Masov, V.; Tagirov, M.; Kuznetsov, D. ; Synthesis, Characterization and Reactivity of Nanostructured Zero-Valent Iron Particles for Degradation of Azo Dyes. *Int. J. Nanosci.* **2017**, *16*, 1750017. [CrossRef]
35. Mikhailov, I.; Komarov, S.; Levina, V.; Gusev, A.; Issi, J.P.; Kuznetsov, D. Nanosized zero-valent iron as Fenton-like reagent for ultrasonic-assisted leaching of zinc from blast furnace sludge. *J. Hazard. Mater.* **2017**, *321*, 557–565. [CrossRef] [PubMed]
36. Turabik, M.; Simsek, U.B. Effect of synthesis parameters on the particle size of the zero valent iron particles. *Inorg. Nano-Met. Chem.* **2017**, *47*, 1033–1043. [CrossRef]
37. Hwang, Y.H.; Kim, D.G.; Shin, H.S. Effects of synthesis conditions on the characteristics and reactivity of nano scale zero valent iron. *Appl. Catal. B Environ.* **2011**, *105*, 144–150. [CrossRef]
38. Han, Y.; Yang, M.D.; Zhang, W.; Yan, W. Optimizing synthesis conditions of nanoscale zero-valent iron (nZVI) through aqueous reactivity assessment. *Front. Environ. Sci. Eng.* **2015**, *9*, 813–822. [CrossRef]

39. Ezzatahmadi, N.; Ayoko, G.A.; Millar, G.J.; Speight, R.; Yan, C.; Li, J.; Li, S.; Zhu, J.; Xi, Y. Clay-supported nanoscale zero-valent iron composite materials for the remediation of contaminated aqueous solutions: A review. *Chem. Eng. J.* **2017**, *312*, 336–350. [CrossRef]
40. Eljamal, R.; Eljamal, O.; Khalil, A.M.; Saha, B.B.; Matsunaga, N. Improvement of the chemical synthesis efficiency of nano-scale zero-valent iron particles. *J. Environ. Chem. Eng.* **2018**, *6*, 4727–4735. [CrossRef]
41. Goldstein, N.; Greenlee, L.F. Influence of synthesis parameters on iron nanoparticle size and zeta potential. *J. Nanopart. Res.* **2012**, *14*, 760. [CrossRef]
42. Woo, H.; Park, J.; Lee, S.; Lee, S. Effects of washing solution and drying condition on reactivity of nano-scale zero valent irons (nZVIs) synthesized by borohydride reduction. *Chemosphere* **2014**, *97*, 146–152. [CrossRef]
43. Glavee, G.N.; Klabunde, K.J.; Sorensen, C.M.; Hadjipanayis, G.C. Chemistry of borohydride reduction of iron (II) and iron (III) ions in aqueous and nonaqueous media. Formation of nanoscale Fe, FeB, and Fe2B powders. *Inorg. Chem.* **1995**, *34*, 28–35. [CrossRef]
44. Ngo, Q.B.; Dao, T.H.; Nguyen, H.C.; Tran, X.T.; Van Nguyen, T.; Khuu, T.D.; Huynh, T.H. Effects of nanocrystalline powders (Fe, Co and Cu) on the germination, growth, crop yield and product quality of soybean (Vietnamese species DT-51). *Adv. Nat. Sci. Nanosci. Nanotechnol.* **2014**, *5*, 015016. [CrossRef]
45. Habish, A.J.; Lazarević, S.; Janković-Častvan, I.; Jokić, B.; Kovač, J.; Rogan, J.; Janaćković, Đ.; Petrović, R.; Petrović, R. Nanoscale zerovalent iron (nZVI) supported by natural and acid-activated sepiolites: The effect of the nZVI/support ratio on the composite properties and Cd 2+ adsorption. *Environ. Sci. Pollut. Res.* **2017**, *24*, 628–643. [CrossRef] [PubMed]
46. Jia, Y.F.; Xiao, B.; Thomas, K.M. Adsorption of metal ions on nitrogen surface functional groups in activated carbons. *Langmuir* **2002**, *18*, 470–478. [CrossRef]
47. Michel, F.M.; Ehm, L.; Antao, S.M.; Lee, P.L.; Chupas, P.J.; Liu, G.; Strongin, D.R.; Schoonen, M.A.; Phillips, B.L.; Parise, J.B. The structure of ferrihydrite, a nanocrystalline material. *Science* **2007**, *316*, 1726–1729. [CrossRef] [PubMed]
48. Drits, V.A.; Sakharov, B.A.; Salyn, A.L.; Manceau, A. Structural model for ferrihydrite. *Clay Miner.* **1993**, *28*, 185–207. [CrossRef]
49. Pullin, H.; Springell, R.; Parry, S.; Scott, T. The effect of aqueous corrosion on the structure and reactivity of zero-valent iron nanoparticles. *Chem. Eng. J.* **2017**, *308*, 568–577. [CrossRef]
50. Liu, A.; Liu, J.; Zhang, W.X. Transformation and composition evolution of nanoscale zero valent iron (nZVI) synthesized by borohydride reduction in static water. *Chemosphere* **2015**, *119*, 1068–1074. [CrossRef]
51. Li, Z.; Sun, T.; Jia, J. An extremely rapid, convenient and mild coal desulfurization new process: Sodium borohydride reduction. *Fuel Process. Technol.* **2010**, *91*, 1162–1167. [CrossRef]
52. Li, F.Y.; Koopal, L.; Tan, W.F. Effect of citrate on the species and levels of Al impurities in ferrihydrite. *Colloids Surf. A Physicochem. Eng. Asp.* **2018**, *539*, 140–147. [CrossRef]
53. Pariona, N.; Camacho-Aguilar, K.I.; Ramos-González, R.; Martinez, A.I.; Herrera-Trejo, M.; Baggio-Saitovitch, E. Magnetic and structural properties of ferrihydrite/hematite nanocomposites. *J. Magn. Magn. Mater.* **2016**, *406*, 221–227. [CrossRef]
54. Xu, H.; Ji, L.; Kong, M.; Jiang, H.; Chen, J. Molecular weight-dependent adsorption fractionation of natural organic matter on ferrihydrite colloids in aquatic environment. *Chem. Eng. J.* **2019**, *363*, 356–364. [CrossRef]
55. Sawafta, R.; Shahwan, T. A comparative study of the removal of methylene blue by iron nanoparticles from water and water-ethanol solutions. *J. Mol. Liq.* **2019**, *273*, 274–281. [CrossRef]
56. Eljamal, O.; Mokete, R.; Matsunaga, N.; Sugihara, Y. Chemical pathways of nanoscale zero-valent iron (NZVI) during its transformation in aqueous solutions. *J. Environ. Chem. Eng.* **2018**, *6*, 6207–6220. [CrossRef]
57. Ma, X.; He, D.; Jones, A.M.; Collins, R.N.; Waite, T.D. Reductive reactivity of borohydride-and dithionite-synthesized iron-based nanoparticles: A comparative study. *J. Hazard. Mater.* **2016**, *303*, 101–110. [CrossRef] [PubMed]
58. Zhao, R.; Zhou, Z.; Zhao, X.; Jing, G. Enhanced Cr (VI) removal from simulated electroplating rinse wastewater by amino-functionalized vermiculite-supported nanoscale zero-valent iron. *Chemosphere* **2019**, *218*, 458–467. [CrossRef]
59. Zhang, S.H.; Wu, M.F.; Tang, T.T.; Xing, Q.J.; Peng, C.Q.; Li, F.; Liu, H.; Luo, X.B.; Zou, J.P.; Luo, J.M.; et al. Mechanism investigation of anoxic Cr (VI) removal by nano zero-valent iron based on XPS analysis in time scale. *Chem. Eng. J.* **2018**, *335*, 945–953. [CrossRef]

60. Joseyphus, R.J.; Shinoda, K.; Kodama, D.; Jeyadevan, B. Size controlled Fe nanoparticles through polyol process and their magnetic properties. *Mater. Chem. Phys.* **2010**, *123*, 487–493. [CrossRef]
61. Logan, S.R. Effects of ionic strength on the rates of reaction between ions in solution. *Trans. Faraday Soc.* **1967**, *63*, 3004–3008. [CrossRef]
62. Yu, C.; Shao, J.; Sun, W.; Yu, X. Treatment of lead contaminated water using synthesized nano-iron supported with bentonite/graphene oxide. *Arab. J. Chem.* **2018**. [CrossRef]
63. Jabeen, H.; Kemp, K.C.; Chandra, V. Synthesis of nano zerovalent iron nanoparticles—Graphene composite for the treatment of lead contaminated water. *J. Environ. Manag.* **2013**, *130*, 429–435. [CrossRef]